Available online at www.sciencedirect.com
SCIENCE DIRECT®
International Journal of Heat and Mass Transfer 47 (2004) 5129–5137
International Journal of HEAT and MASS TRANSFER
www.elsevier.com/locate/ijhmt

Effects of void-induced convection on interface morphology and segregation during low-g solidification

S. Barsi [a], M. Kassemi [b,*], J.I.D. Alexander [a]

[a] Department of Mechanical Engineering, Case Western Reserve University, Cleveland, OH 44106, USA
[b] National Center for Microgravity Research, NASA Glenn Research Center, 21000 Brookpark Road, MS110-3, Cleveland, OH 44135, USA

Received 6 August 2003; received in revised form 20 May 2004
Available online 11 August 2004

Abstract

Recent microgravity experiments have been hampered by convection caused by unwanted voids and/or bubbles in the melt. In this work, a numerical model is developed to describe how thermocapillary convection generated by a void can affect a typical Bridgman solidification process in microgravity. The model is based on the quasi-steady Navier–Stokes equations for a Newtonian fluid coupled with the conservation equations for transport of energy and species. Numerical solutions for a variety of operating conditions indicate that void-generated thermocapillary convection can have a drastic effect on both interface morphology and solutal transport.
© 2004 Elsevier Ltd. All rights reserved.

Keywords: Solidification; Microgravity; Materials processing; Segregation; Thermocapillary convection; Bubbles; Numerical modeling

1. Introduction

With the advent of the modern electronics industry, semiconductors have become a mainstay of everyday life. Central to the utility of semiconductors is the ability of manufacturers to alter the properties of the crystalline material to meet the specific needs of each technological application. This is usually accomplished through addition of dopants during the crystal growth process. A measure of the quality of the final semiconductor is the uniformity of dopant in the grown crystal [1]. Compositional non-uniformities can make it difficult to achieve certain desirable physical properties in the bulk material [2] and can limit reproducibility of wafer properties in a given crystal. Dopant transport in the melt of the growing crystal is seen to be largely responsible for the compositional inhomogeneities.

Assuming a planar growth interface, Tiller et al. [3] derived an equation governing the solute distribution, or segregation, in the melt region of a directionally solidifying crystal for a diffusion dominated growth process. Their results indicated that, after neglecting an initial and final transient, a significant portion of the solid crystal would grow at a uniform composition. Coriell and Sekerka [4] extended the analysis of Tiller by showing that diffusion controlled growth in the presence of a non-planar growth front can lead to significant levels of solute segregation. Studying growth processes that were not diffusion-controlled, Burton et al. [5] and Wagner [6] showed that convection present in the melt region will drastically affect the uniformity of solutal concentration in the solid.

Of course, convection in the melt will not only affect solutal transport, but can also affect heat transport and, thus, interface morphology. Controlling the levels of convection in the melt region is a difficult task. In many

* Corresponding author. Tel.: +1-216-433-5031; fax: +1-216-433-5033.
E-mail address: mohammad.kassemi@grc.nasa.gov (M. Kassemi).

0017-9310/$ - see front matter © 2004 Elsevier Ltd. All rights reserved.
doi:10.1016/j.ijheatmasstransfer.2004.05.024

Nomenclature

C	concentration
c_p	specific heat (J/kg K)
D	diffusion coefficient (m^2/s)
H	mean curvature (1/m)
k	thermal conductivity (W/m K)
L	latent heat (J/kg)
l	void-interface distance (m)
$\hat{n}$	unit normal vector
P	pressure (N/m^2)
R	residual vector
S	solution vector
T	temperature (K)
$\hat{t}$	unit tangent vector
$\vec{V}$	velocity (m/s)

Greek symbols

δ	interface deflection (m)
ε	tolerance
κ	partition coefficient
μ	dynamic viscosity (kg/m s)
ρ	density (kg/m^3)
σ	stress (N/m^2)
ψ	stream function (m^2/s)

Subscripts

g	growth
I	interface
l	liquid
n	normal
R	residual
r	radial direction
S	solution
s	solid
t	tangent
z	axial direction

cases this is because natural convection, driven by buoyancy forces resulting from thermally and/or solutally generated density variations in the bulk of the melt, is difficult to avoid and can strongly affect transport conditions. Significant levels of convection during the crystal growth process are encountered even when a crystal is grown in a thermally stable Bridgman configuration [7,8]. These natural convective flows originate from density variations induced often by quite small, but unavoidable radial temperature gradients in the melt, which are due to a mismatch in thermal conductivities of the solid, melt and ampoule.

To eliminate the undesirable effects of natural convection, it seems advantageous to carry out these crystal growth processes in a weightless environment provided by orbiting spacecraft. However, in microgravity environments, other problems, which are masked by strong buoyancy on earth, can become important.

A problem often encountered in microgravity crystal growth experiments has been evolution of bubbles and voids in the melt during the growth process. As a result, post-growth analysis of several recent microgravity experiments [9–11] have revealed a considerable number of voids/bubbles present in the space grown crystals.

As an example, in the selenium-doped gallium arsenide microgravity experiment [9] a significant number of voids were found in the solid crystal. Results suggested that dopant transport was dominated by convection rather than diffusion during growth. Kassemi et al. [12,13] have hypothesized that this convective mixing of solute was due to the thermocapillary flow generated by voids in the gallium arsenide melt. Thermocapillary convection is driven by surface tension gradients, which are generated by temperature variations along a free surface. Pimputkar and Ostrach [14] first called attention to the importance of understanding thermocapillary flows especially as it pertains to crystal growth. In this context, Kassemi et al. [12,13] showed how a typical microgravity crystal growth process can be affected by thermocapillary convection. Their results indicated that void-generated convection can have a significant impact on interfacial segregation patterns especially if the void is located close the growth interface. In these studies [12,13] attention focused on the melt region alone by invoking a simplifying assumption that the interface shape is fixed. The interface shape in previous models was extracted from space experiments [9]. In this work, we extend the previous models to account for the possibility that the interface will change shape, thus changing heat and mass transfer conditions in the melt.

2. Mathematical formulation

In this work, a numerical model is developed to describe how thermocapillary convection generated by a void or bubble can affect microgravity solidification of a dilute binary alloy. Specifically, the growth of selenium-doped gallium arsenide (GaAs) is studied. A schematic of the growth configuration indicating the solid, melt, ampoule and wall regions as well as their relationship to the three zone Bridgman furnace is shown in Fig. 1.

The flow in the melt is described by the continuity and momentum equations:

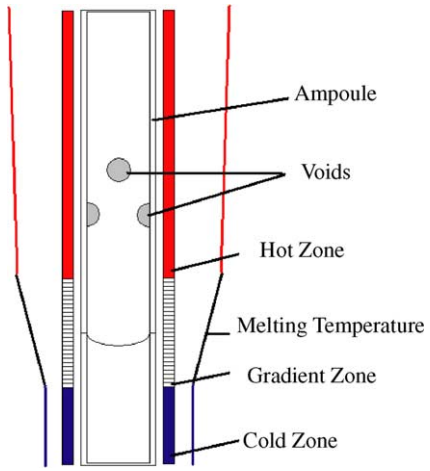

Fig. 1. Schematic of the growth configuration.

$$\nabla \cdot \vec{V} = 0 \tag{1}$$

$$\rho(\vec{V} \cdot \nabla \vec{V}) = -\nabla P + \mu \nabla^2 \vec{V} \tag{2}$$

In order to represent the crystal growth process, the pseudo-steady-state approach [15,16] is employed. The continuous steady growth process and movement of the interface are accommodated by letting mass enter at the hot end of the ampoule at the growth velocity V_g and uniform composition C_0 and removing crystal from the cold end at a velocity that conserves total mass in the system. Therefore, the velocity boundary conditions at the hot and cold ends of the ampoule are

$$\vec{V}_{\text{top}} = V_g \hat{n}_z, \quad \vec{V}_{\text{bot}} = \frac{\rho_l}{\rho_s} V_g \hat{n}_z \tag{3}$$

where $\hat{n}_z$ points from the hot end to the cold end of the ampoule.

A no-slip condition is applied at the ampoule side wall:

$$\vec{V} = V_g \hat{n}_z \tag{4}$$

The transport of heat is governed by the equation for conservation of energy:

$$\rho c_p(\vec{V} \cdot \nabla T) = k \nabla^2 T \tag{5}$$

At the top, bottom, and side walls of the ampoule, prescribed temperature boundary conditions are applied:

$$T_{\text{top}} = T_h, \quad T_{\text{bot}} = T_c, \quad T = T(z) \tag{6}$$

The surface of the void is taken to be adiabatic:

$$\nabla T \cdot \hat{n} = 0 \tag{7}$$

The transport of solute is governed by the equation for conservation of species:

$$\rho(\vec{V} \cdot \nabla C) = \rho D \nabla^2 C \tag{8}$$

The species boundary condition at the top of the domain is

$$C_{\text{top}} = C_0 \tag{9}$$

where C_0 is a bulk reference concentration.

A zero flux concentration boundary condition is applied to the bottom boundary:

$$\left.\frac{\partial C}{\partial z}\right|_{\text{bot}} = 0 \tag{10}$$

Finally, the ampoule wall and void–melt interface are assumed to be impermeable to the solute:

$$\nabla C \cdot \hat{n}_r = 0 \tag{11}$$

For heat and mass transfer across the solid–melt interface additional conditions are needed. The thermal boundary condition applied to the interface is given by

$$T_l = T_s = T_I \tag{12}$$

The above condition implies that thermal equilibrium exists across the interface such that the temperature of the liquid side of the interface is equal to the temperature on the solid side of the interface.

An energy flux balance across the interface results in the difference in heat fluxes on the solid and liquid sides of the interface equaling the amount of latent heat liberated at the interface:

$$k_l \nabla T_l \cdot \hat{n} - k_s \nabla T_s \cdot \hat{n} = \rho_s L(\vec{V}_s - \vec{V}_I) \cdot \hat{n} \tag{13}$$

A mass flux balance across the interface yields

$$\rho_l(\vec{V}_l - \vec{V}_I) \cdot \hat{n} = \rho_s(\vec{V}_s - \vec{V}_I) \cdot \hat{n} \tag{14}$$

A no-slip condition applied to the interface results in

$$(\vec{V}_l - \vec{V}_s) \cdot \hat{t} = 0 \tag{15}$$

To model solute segregation, the mass conservation of solute across the growth interface is given by

$$\rho_s C_s(\vec{V}_s - \vec{V}_I) \cdot \hat{n} - \rho_l C_l(\vec{V}_l - \vec{V}_I) \cdot \hat{n} = (\rho_l D_l \nabla C_l - \rho_s D_s \nabla C_s) \cdot \hat{n} \tag{16}$$

Finally, a thermodynamic relationship between solute on the liquid side of the interface and solute on the solid side of the interface is given by

$$C_s = \kappa C_l \tag{17}$$

where κ is the partition coefficient. In Eqs. (12)–(17) the unit normal vector points into the solid.

Along the free surface of the void, a normal and tangential stress balance is applied:

Table 1
GaAs properties and system parameters

Dynamic viscosity	0.0042 kg/m s
Liquid thermal conductivity	17.8 W/m K
Liquid specific heat capacity	435 J/kg K
Liquid density	5720 kg/m^3
Thermal volume expansion coefficient	1.87×10^{-4} K^{-1}
Surface tension [17]	1.67–0.00096T N/m
Liquid diffusion coefficient	2×10^{-9} m^2/s
Solid thermal conductivity	7.1 W/m K
Solid specific heat capacity	418 J/kg K
Solid diffusion coefficient	2×10^{-13} m^2/s
Solid density	5160 kg/m^3
Latent heat	7.27×10^5 J/kg
Partition coefficient	0.10
Growth rate	2.5×10^{-6} m/s
Void radius	0.0044 m
Ampoule radius	0.0075 m
Ampoule length	0.165 m
Shallow temperature gradient	34.783 K/m
Steep temperature gradient	1500 K/m
T_m	1511 K
T_c	1496 K
Length of steep gradient zone	0.02 m
Ampoule wall thickness	0.000889 m
Density of ampoule	2150 kg/m^3
Specific heat of ampoule	791 J/kg K
Thermal conductivity of ampoule (radial dir.)	5 W/m K
Thermal conductivity of ampoule (axial dir.)	60 W/m K

$$\sigma_n = 2\gamma H - P_a \tag{18}$$

$$\sigma_t = \nabla\gamma \cdot \hat{t} \tag{19}$$

The relevant thermophysical properties of gallium arsenide are available in the literature [12,13] and are listed along with some system parameters [9] in Table 1.

3. Solution methodology

The problem is solved numerically using a customized version of the FIDAP finite element code. In the model, the shapes of the growth interface and the void interface are not known a priori. Consequently, both the solid–melt and void–melt interfaces are modeled as moving boundaries that are updated at each step.

Along the void–melt interface the balance of normal and tangential stresses along the interface is used to satisfy boundary conditions in the momentum equation and the kinematic constraint is used to update the location of the free surface. To simplify the present analysis, the shape of the void, as well as its location in the melt region, is assumed fixed. Therefore, the simulations presented herein can be regarded as snapshots in time as the solidification process proceeds.

The shape of the void is fixed by setting the normal velocities of nodes on the surface of the void to zero. The position of the void is fixed by setting the velocities at the void tips to zero and by fixing the contact angle between the void and either the line of symmetry or the ampoule wall (depending on whether the void is located along the central axis or along the side wall, respectively). For the present phase change problem, the balance of energy flux across the growth interface (Eq. (13)) is used to update the position of the nodes lying along the interface.

The solution is obtained in two steps. In the first step, the global system of equations for continuity, energy, and momentum is solved in a pseudo-transient manner by marching out in time to a steady state solution using a first order backward Euler integration scheme. At each time step, the continuity, energy, and momentum equations are solved sequentially using a segregated Gaussian elimination solver. The pseudo-transient solutions were obtained by starting from a field in conductive equilibrium subjected to a uniform pulling velocity with an initially planar interface. Since solutal buoyancy and solutal dependencies on the melting temperature are negligible, the species conservation equation is completely decoupled from the energy and momentum equations. Therefore, in the second step, the conservation equation for the solute can be solved separate from the other conservation equations. The species equation is obtained using Gaussian elimination with solutions of velocity, temperature, interface shape, and mesh geometry generated in the first step as input to the steady state solver.

To arrive at a converged solution, two convergence criteria must be satisfied simultaneously. These criteria are

$$\left\| \frac{S_i - S_{i-1}}{S_i} \right\| \leqslant \varepsilon_S \tag{20}$$

$$\left\| \frac{R_i}{R_0} \right\| \leqslant \varepsilon_R \tag{21}$$

where S_i and R_i are respectively the solution and residual force vectors at iteration i. The norm $\|\cdot\|$ is the root-mean-square norm summed over all of the equations. For both criteria, the tolerances, ε_S and ε_R, were set to 0.0001. In addition to the above two criteria, when solving for the position of the growth interface, an additional convergence criteria is needed:

$$\|\delta_i\| \leqslant \varepsilon_\delta \tag{22}$$

Table 2
Grid resolution results for the void-in-center configuration

l	Variable	542 Elements	1082 Elements	1357 Elements
0.0456 m	V_{max}	0.006159	0.006163	0.006163
		(0.065)	(0)	
	$\|\psi\|_{max}$	8.5819×10^{-6}	8.7875×10^{-6}	8.7598×10^{-6}
		(2.03)	(0.316)	
	C_{max}	5.64036	5.94302	5.98188
		(5.709)	(0.649)	
	T	1527.41172	1527.41198	1527.41200
		$O(10^{-5})$	$O(10^{-6})$	
	δ	0.0029576	0.0030741	0.0030891
		(4.257)	(0.485)	
0.0050 m	V_{max}	0.07276	0.07028	0.07057
		(3.103)	(0.411)	
	$\|\psi\|_{max}$	6.8125×10^{-5}	7.4389×10^{-5}	7.4497×10^{-5}
		(8.553)	(0.145)	
	C_{max}	1.25732	1.31039	1.30822
		(3.891)	(0.166)	
	T	1522.10064	1522.12970	1522.13974
		$O(10^{-3})$	$O(10^{-4})$	
	δ	0.0120150	0.0122446	0.0122499
		(1.918)	(0.043)	

where $\|\delta_i\|$ is the norm of the free surface deflection at iteration i. In the present model, the tolerance for surface deformation is also specified to be 0.0001. To give an indication of the convergence behavior of the solution method, when the bubble is located on the sidewall at $l = 4.56$ cm, a steady-state was achieved in the first step after marching out approximately 10,000 seconds. The species equation converged after 26 iterations for this void configuration.

The solutions generated in this paper are generated using approximately 1357 nine-node quadratic elements (4397 nodes) with a dense clustering of nodes near the solid–melt and void–melt interfaces. Grid independence is checked by comparing solutions generated on two coarser meshes with solutions generated on the finest mesh. Table 2 presents grid convergence results for when the void is located in the high temperature gradient region and the low temperature gradient region for the void-in-center configuration. The quantity in parentheses represents the percentage difference between the solution parameters generated on the coarser grids with those generated on the finest grid. The comparisons indicate excellent grid resolution for all the designated solution parameters.

4. Results and discussion

In order to investigate the effects of void-generated thermocapillary convection on a microgravity solidification process, a void is placed in the melt phase of a dilute binary alloy. By using a quasi-steady approach and by varying the axial distance between the void and the solid–melt interface (denoted by l in subsequent sections) the effects of void-generated convection on interface morphology and solute segregation can be studied.

In the present analysis, two void configurations are considered. Post-growth examination of the solid sample from the space experiment [9] showed a considerable number of voids located along the central axis of the ampoule. But upon careful examination, Kaforey et al. [18] suggested that the voids most likely formed at the ampoule wall during the charge-melting interval and were later swept to the center of the ampoule during the solidification process. Furthermore, because the initial pre-melt solid samples consisted of three distinct charges, they postulated that the voids were initially in form of annular regions attached to the crucible at the location of the original solid charge boundaries. It is not clear when the void detachment from the wall and movement to the center of the crucible occurred. Therefore, in order to accommodate all possibilities, two sets of axisymmetric simulations are performed. In the first set, the void is hemispherical and at the center of the ampoule. In the second set, the void is represented by an annular region attached to the ampoule wall.

Because the void in the present growth configuration is exposed to an external temperature gradient and the surface tension of gallium arsenide is a decreasing function of temperature, there will be a surface tension

gradient acting along the void–melt interface. This surface tension gradient results in a tangential stress (Eq. (19)), which acts along the surface of the void and tends to pull warmer fluid down along the void's surface toward the melt interface. Clearly, if the resulting thermocapillary vortex is close to the melt interface, transporting warmer fluid to that interface can affect the temperature field in the ampoule and thus the shape of the growth front.

Interface deflections for the two void configurations are shown in Fig. 2. For each of these configurations, even when the void is located far from the interface ($l = 0.0456$ m) there is still significant interface deflection. At 0.0456 m away from the interface, as Figs. 3 and 4 indicate, the void-generated thermocapillary vortex has not reached the solid–melt interface. Thus, the resulting interface deflection cannot be attributed to thermocapillary convection, and is solely due to the mismatch in thermal conductivities between the solid, melt, and ampoule.

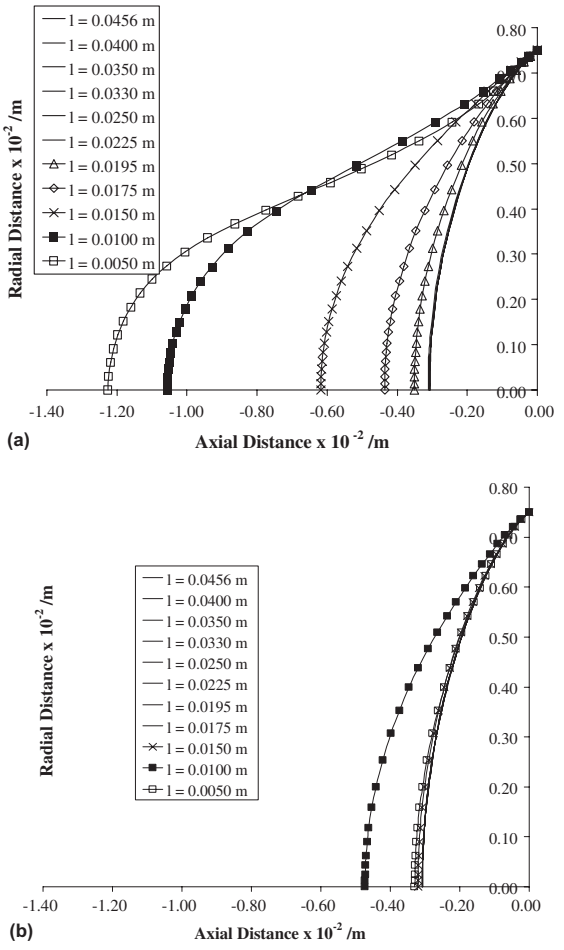

Fig. 2. Interface deflections for different void configurations: (a) void-in-center, (b) void-on-side.

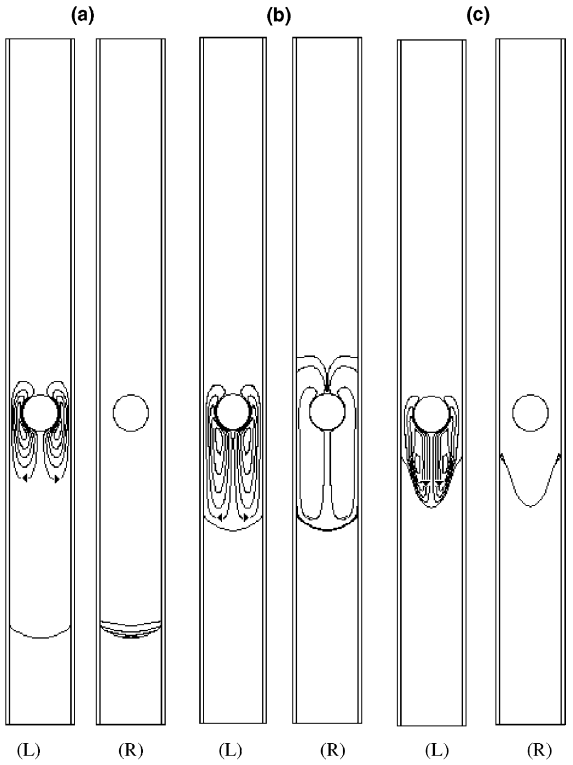

Fig. 3. Streamlines (L) and isoconcentration lines (R) for the void-in-center configuration: (a) $l = 0.0456$ m [5 contours, $\psi_{max} = 0.0$ and $\psi_{min} = -8.7598 \times 10^{-6}$; 5 contours, $C_{max} = 5.9819$ and $C_{min} = 0.0$]; (b) $l = 0.0195$ m [5 contours, $\psi_{max} = 0.0$ and $\psi_{min} = -1.7170 \times 10^{-5}$; 5 contours, $C_{max} = 1.9898$ and $C_{min} = 0.0$]; (c) $l = 0.0050$ m [5 contours, $\psi_{max} = 8.0612 \times 10^{-8}$ and $\psi_{min} = -7.4497 \times 10^{-5}$; 5 contours, $C_{max} = 1.30822$ and $C_{min} = 0.0$].

Fig. 2a shows that for the void-in-center configuration there is a drastic effect on interface deflection as the distance between the void and the solid–melt interface decreases. When the void is located 0.0050 m away from the growth front, the resulting deflection is four times greater than if the void were located 0.0456 m away from the interface. Streamlines in Fig. 3c show for the $l = 0.0050$ m void-in-center configuration, the thermocapillary vortex has reached the interfacial region. The effect of bringing warmer fluid towards the interface causes additional melting which results in the drastic stretching of the interface as depicted in Fig. 2a.

Different behavior arises when the void is located on the side wall. Fig. 2b shows interface deflections for the void-on-side configuration. For the $l = 0.0456$ m case, the deflection is identical to the void-in-center $l = 0.0456$ m case; as it should be. At this distance away from the growth front, it is a thermal conductivity mismatch

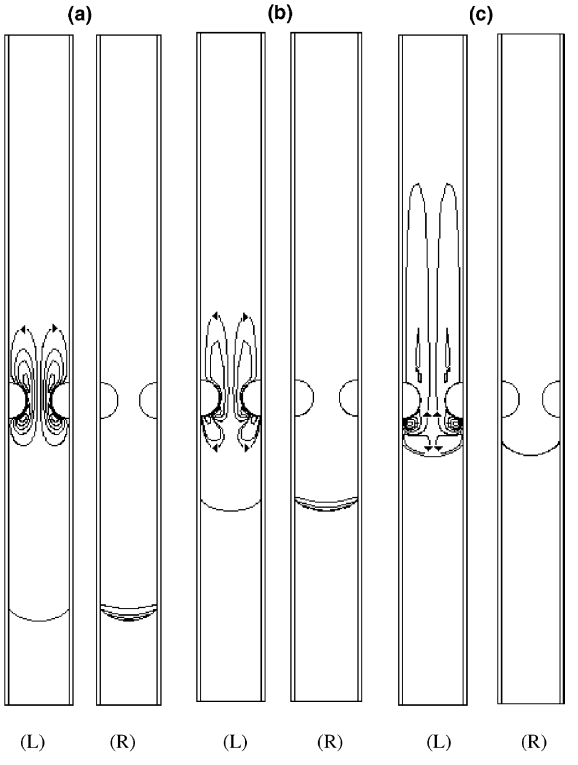

Fig. 4. Streamlines (L) and isoconcentration lines (R) for the void-on-side configuration: (a) $l = 0.0456$ m [5 contours, $\psi_{max} = 8.4626 \times 10^{-6}$ and $\psi_{min} = 5.9407 \times 10^{-7}$; 5 contours, $C_{max} = 6.2137$ and $C_{min} = 0.0$]; (b) $l = 0.0195$ cm [6 contours, $\psi_{max} = 1.6102 \times 10^{-5}$ and $\psi_{min} = -9.544 \times 10^{-6}$; 5 contours, $C_{max} = 5.7683$ and $C_{min} = 0.0$]; (c) $l = 0.0050$ m [6 contours, $\psi_{max} = 1.3465 \times 10^{-4}$ and $\psi_{min} = -7.8732 \times 10^{-6}$; 5 contours, $C_{max} = 1.3372$ and $C_{min} = 0.0$].

rather than any thermocapillary effect that causes deformation of the solidification front.

Unlike the void-in-center configuration, when the void is located on the side wall for the $l = 0.0195$ m case, the resulting thermocapillary flow does not reach the interfacial region and therefore the shape of the interface is unaffected by the flow. This can be seen by comparing Figs. 3b and 4b. The streamline contours depicted in Figs. 3b and 4b reveal that the penetration depth of the thermocapillary vortex is much shorter for the void-on-side configuration than it is for the void-in-center configuration. This is because for the void-on-side configuration, there is friction imparted to the fluid as the thermocapillary vortices flow along the ampoule wall. In Fig. 4c, when the bubble is located 0.0050 m away from the melt-interface, a secondary shear-driven vortex develops between the interface and the main thermocapillary driven vortex. This shear-driven vortex prevents the thermocapillary vortex from ever reaching the interface. Consequently, the deflection of the interface is smaller for the $l = 0.0050$ m case than the deflection resulting when the void-interface distance is 0.0100 m.

In addition to affecting interface morphology, void-induced thermocapillary convection also affects solutal transport during the crystal growth process. The effects of thermocapillary convection on the solute concentration field is shown for the void-in-center configuration in Fig. 3. Fig. 3a shows a solute-rich region on the liquid side of the interface as a result of solute rejection at the interface. This is a consequence of the segregation coefficient of gallium arsenide being less than unity—solute will be rejected at the growth front into the liquid. When the void is far from the interface ($l = 0.0456$ m), the thermocapillary vortex has not penetrated the solutal build-up region. Thus, transport of solute at the growth front is dominated by diffusion. In contrast, at $l = 0.0195$ m, the thermocapillary vortex generated by the void has reached the growth front. The vortex is sweeping solute away from the center of the interface towards the side walls. At $l = 0.0050$ m (Fig. 3c) away from the melt interface, the void is now in the steep temperature gradient region. In a steeper temperature gradient, the velocities generated along the surface of the void will be larger. The strong thermocapillary flow for the $l = 0.0050$ m case wipes out the solutal boundary layer at the growth interface which results in complete mixing of the solute and leads to a uniform solutal concentration in the melt.

Evolution from a diffusion-dominated regime to a complete mixing regime is shown for the void-in-center configuration in Fig. 5. The curves represent radial interfacial solute distributions for different void-interface distances. Note that the curves are of different length due to the stretching of the interface resulting from convection as the void approaches the two-phase front. When the void-interface distance is large, there is a solutal build-up in the center of the interface. This is a consequence of interfacial curvature rather than any flow-induced phenomena. As the void moves closer to the interface (at $l = 0.0225$ m, for example) the concentration is beginning to become more uniform as a result of convective mixing. The thermocapillary vortex is sweeping solute away from the center of the interface towards the wall. As the void-interface distance continues to decrease, any solutal boundary layer that existed is wiped out by the thermocapillary flow resulting in a nearly uniform concentration along the interface. Similar results are shown in Fig. 6 for when the void is located along the ampoule wall.

The results of this analysis can be succinctly summarized by plotting the radial segregation along the interface as a function of void-interface distance (Fig. 7). The curves indicate three distinct regions. For the two void configurations, at large void-interface distances, the thermocapillary vortex does not penetrate

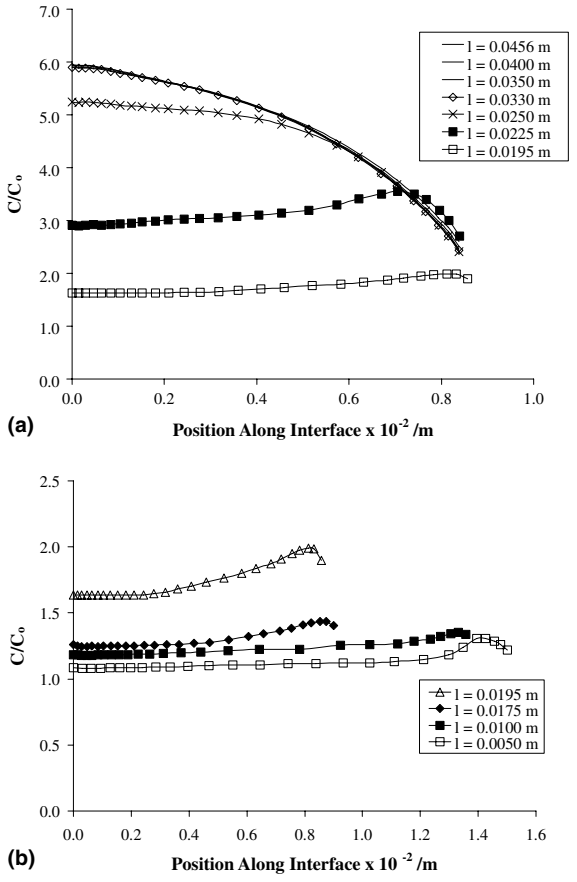

Fig. 5. Dopant concentration along the melt interface for the void-in-center configuration.

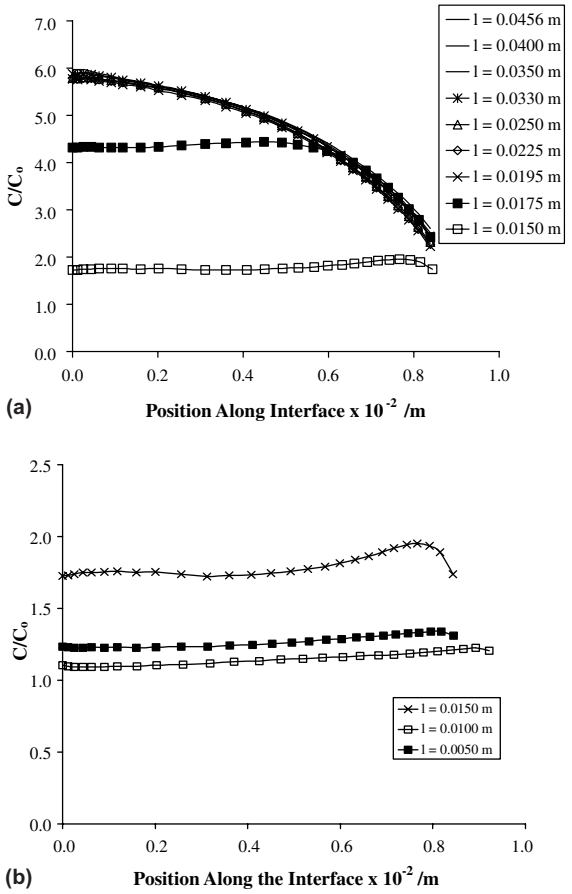

Fig. 6. Dopant concentration along the melt interface for the void-on-side configuration.

the solute-rich region on the melt side of the interface. Segregation along the interface is therefore a consequence of diffusion normal to the curved interface and not of any convective phenomena. Since the curvature of the interface is independent of the flow when the void-interface distance is large, the void-on-side and void-in-center configurations result in nearly identical levels of radial segregation.

Fig. 7 also shows a transitionary region where the mechanism for solute transport shifts from a diffusion-dominated process to one characterized by convective mixing. This transitionary region occurs when the flow just penetrates the solute-rich region on the melt side of the interface. Fig. 7 reveals that the transition occurs later for the void-on-side configurations. This is a result of friction imparted by the wall, which reduces the penetration depth of the thermocapillary vortex when the void is located along the ampoule wall.

Finally in Fig. 7, the radial segregation along the interface is drastically mitigated for small void-interface distances. In this region, intense thermocapillary flow wipes out the solutal boundary layer resulting in a nearly

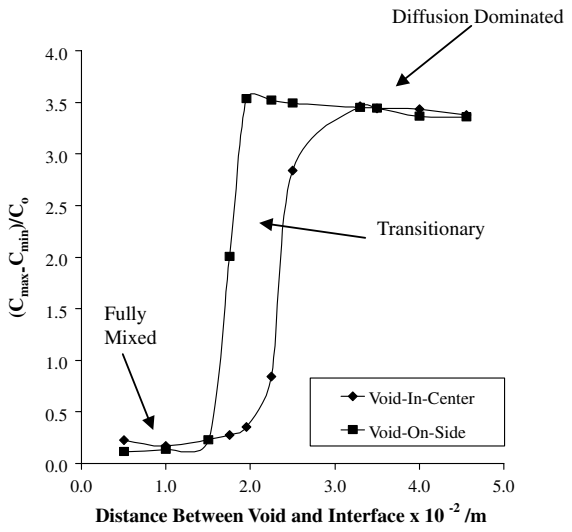

Fig. 7. Radial segregation as a function of void-interface distance.

uniform concentration along the interface. Transport of solute for this region can be described by a complete mixing regime.

5. Conclusions

In this work, the effects of void-induced thermocapillary convection on heat and mass transport during microgravity solidification of selenium-doped gallium arsenide are investigated. By varying the axial distance between the void and the solid–melt interface for two different void configurations some general conclusions can be drawn. Regardless of the void configuration, when the distance between the void and the interface is large, departure from an initially planar interface is attributed to a mismatch between the thermal conductivities of the solid, melt, and ampoule. As the distance between the void and the solid–melt interface is decreased, thermocapillary convection, driven by surface tension gradients along the free surface of the void, brings warmer fluid from the top of the ampoule towards the interface. This depresses the melting point isotherm. As a result, the solid–melt interface deflects more than it would if the void were located farther away. For the void-on-side configurations, because of friction imparted to the fluid by the wall and the development of shear-driven vortices at small void-interface distances, the interface deflections are less than the corresponding deflections in the void-in-center configuration.

Void-generated thermocapillary convection can also have a profound effect on the solute concentration field in the melt. When the distance between the void and solid–melt interface was far, the resulting thermocapillary vortex did not penetrate the solute-rich region on the melt side of the interface. Any resulting segregation along the growth interface was due to diffusion and interface curvature and not to convection. As the thermocapillary vortex reaches the solutal build-up region, the flow sweeps the solute away from the interface. When the void is very close to the interface, the flow can completely wipe out the solutal boundary layer and a nearly uniform concentration field in the melt is established. Thus, as the distance between the void and the solid–melt interface decreases, the growth process changes from a diffusion-controlled process to a weak mixing regime and finally to a complete mixing regime. The regime changes occur at greater bubble—melt-interface distances for the void-in-center configuration than for both of the void-on-side configurations.

References

[1] R.A. Brown, Theory of transport processes in single crystal growth from the melt, AIChE J. 34 (6) (1988) 881–911.
[2] J.R. Carruthers, Crystal growth in a low gravity environment, J. Crystal Growth 42 (1977) 379–385.
[3] W.A. Tiller, K.A. Jackson, J.W. Rutter, B. Chalmers, The redistribution of solute atoms during the solidification of metals, Acta Metallurgica 1 (1953) 428–437.
[4] S.R. Coriell, R.F. Sekerka, Lateral solute segregation during unidirectional solidification of a binary alloy with a curved solid–liquid interface, J. Crystal Growth 46 (1979) 479–482.
[5] J.A. Burton, R.C. Prim, W.P. Slichter, The distribution of solute in crystals grown from the melt. Part I: Theoretical, J. Chem. Phys. 21 (11) (1953) 1987–1991.
[6] C. Wagner, Theoretical analysis of diffusion of solutes during the solidification of alloys, J. Metals 6 (1954) 154–160.
[7] R.K. Crouch, A.L. Fripp, W.J. Debnam, I.O. Clark, F.M. Carlson, Ground based studies for the space processing of lead tin telluride, in: G.E. Rindone (Ed.), Materials Processing in the Reduced Gravity Environment of Space, North-Holland, New York, 1982, pp. 611–618.
[8] S.L. Lehoczky, F.R. Szofran, Directional solidification and characterization of $Hg_{1-x}Cd_xTe$ alloys, in: G.E. Rindone (Ed.), Materials Processing in the Reduced Gravity Environment of Space, North-Holland, New York, 1982, pp. 409–420.
[9] D.H. Matthiesen, J.A. Majewski, The study of dopant segregation behavior during the growth of GaAs in microgravity, Joint "L+1" Science Review for USML-1 and USMP-1 with the Microgravity Measurement Group, 1993.
[10] A.L. Fripp, W.J. Debnam, G.A. Woodell, W.R. Rosch, R. Narayanan, The effect of microgravity direction on the growth of PbSnTe, Technical Paper AIAA 97-0676, 1997.
[11] J.B. Andrews, L.J. Hayes, Y. Arikawa, S.R. Coriell, Microgravity solidification of Al–In alloys, Mater. Sci. Forum 329/330 (2000) 247–258.
[12] M. Kassemi, S. Barsi, M. Kaforey, D. Matthiesen, Effect of void location on segregation patterns in microgravity solidification, J. Crystal Growth 225 (2001) 516–521.
[13] M. Kassemi, M. Kaforey, D. Matthiesen, Effect of void generated thermocapillary convection on dopant segregation in microgravity solidification, J. Thermophys. Heat Transfer 15 (2) (2001) 219–227.
[14] S.M. Pimputkar, S. Ostrach, Convective effects in crystals grown from melts, J. Crystal Growth 55 (1981) 614–646.
[15] M. Yao, A. Chait, A.L. Fripp, W.J. Debnam, Numerical simulation of Bridgman crystal growth of PbSnTe in microgravity, Microgravity Sci. Tech. 8 (4) (1995) 214–225.
[16] P.M. Adornato, R.A. Brown, Convection and segregation in directional solidification of dilute and non-dilute binary alloys: effects of ampoule and furnace design, J. Crystal Growth 80 (1987) 155–190.
[17] R. Shetty, R. Balasubramanian, W.R. Wilcox, Surface tension and contact angle of molten semiconductor compounds, J. Crystal Growth 100 (1990) 58–62.
[18] M.L. Kaforey, J.M. Bly, D.H. Matthiesen, Void formation in gallium arsenide crystals growth in microgravity, J. Crystal Growth 174 (1997) 112–119.